Simulation of coarsening of inter-lath cementite in a Q&T steel during tempering

Yulin Ju [a,c], Claire Davis [b], Martin Strangwood [a,b]

[a] School of Metallurgy and Materials, University of Birmingham, Birmingham, UK.
[b] Warwick Manufacturing Group, University of Warwick, Coventry, UK.
[c] School of Materials Science & Engineering, Jiangsu University, Zhenjiang, China.

Abstract: A mathematical model, using the finite difference approach, was established to consider tempering in a low carbon low alloy quenched and tempered steel based on experimental observations, treating the coarsening of a larger particle and dissolution of a smaller particle as a continuous and simultaneous process for coupled inter-lath cementite systems. The diffusion of Mn was simplified as a 1D diffusion and occurred between the interface elements and their adjacent elements in the model. The mathematical model predicted the shortest dissolution times for smaller particles in coupled inter-lath cementite systems, which agreed well with experimental observations on tempering from 2 to 4 hours. However, the larger particle coarsening was under predicted due to the simplification of considering two particle arrangements.

1. Introduction

The industrial importance of quenched and tempered (Q&T) steel grades means that optimisation of composition and processing combinations for a range of thicknesses is needed. Simulation of microstructural development through the process can aid this optimisation and, to this end, a number of models for tempering have been developed and reported. An earlier study by the authors [1] has identified the composition, structure and overall coarsening rates of carbides in three low carbon, low alloy quenched and tempered steels. One important aspect from that work is that inter-lath

and intra-lath carbides coarsen independently (at least for tempering at 600 °C for up to 16 hours) so that their coarsening behaviour can be simulated separately. Theoretical approaches to simulate the coarsening of precipitates on grain/subgrain boundaries have been proposed by Speight [2], Kirchner [3] and Ardell [4], where the mean field method with a radius distribution function was used to derive Equations 1 - 3. Speight [2] and Kirchner [3] firstly proposed Equation 1 for high-angle grain boundary particle coarsening. The particle shape was assumed to be two symmetrical hemispherical caps along the grain boundary and the mass transfer was assumed to occur in a two - dimensional boundary plane with isotropic diffusion under steady state conditions.

$$r^4 - r_0^4 = Kt$$

$$K = \frac{9\lambda\omega D_{g.b} N_{g.b} V_m}{32ABRT}; \quad A = 2/3 + (\lambda_{g.b}/2\lambda) + (1/3)(\lambda_{g.b}/2\lambda)_3; \quad B = (1/2)\ln(1/f_b)$$

Equation 1

Where r_0 is the initial particle radius; r is the particle radius at time t; K is the rate constant for particle coarsening; $D_{g.b}$ is the solute grain boundary diffusivity; ω is the grain boundary thickness; λ is the interfacial energy between particle and matrix; V_m is the precipitate molar volume; $N_{g.b}$ is the equilibrium solubility at the grain boundary; $\lambda_{g.b}$ is the grain boundary energy; f_b is the fraction of the grain boundary covered by particles. In addition, Ardell [4] expanded the theory for coarsening of precipitates along subgrain boundaries where solute pipe diffusion along dislocations for spherical precipitates in the 2D subgrain boundary plane was the sole diffusion mechanism for mass transfer. Based on the relationship between precipitate radius r and dislocation spacing h, the growth law was divided as:

(a) r >> h (or the misorientation angle is very large)

$$r^4 - r_0^4 = Kt$$

$$K = \frac{64q D_d N_d \lambda \eta V_m}{27\pi hRT} t$$

Equation 2

(b) r ≈ h

$$r^5 - r_0^5 = Kt$$

$$K = \frac{0.311q D_d N_d \lambda N V_m}{\pi RT} t$$

Equation 3

Where q is the cross-section of dislocations that transports the flux of solute atoms; D_d is the dislocation pipe diffusion coefficient; N_d is the solubility of atoms in dislocations in equilibrium with a precipitate of infinite radius; η is a function of the precipitate volume fraction; h is the dislocation spacing, which is associated with the misorientation angle θ; N is the total number of dislocations intersecting with precipitates. The particle volume fraction is ignored in this theoretical analysis; however, the particle diffusion field (radius) decreases with an increase in volume fraction, which leads to an increase of coarsening rate constant (even at very small volume fractions) [5, 6]. In plain and alloyed martensitic steels, coarsening of cementite on grain / lath boundaries is reported to obey the time dependent power growth law $r=Kt_{1/4}$ (for particles on the grain boundary) or $r=Kt_{1/5}$ (for particles on the subgrain boundary), however, the accurate rate constant K values remain unknown in these steels due to the lack of measured parameters to use in Equations 1 - 3 to further fit experimental coarsening data [7 - 9]. Therefore, a theoretical model using data based on experimental analysis is needed to quantitatively simulate the coarsening of carbides on grain/subgrain boundaries during tempering in martensitic steels.

More recently a DICTRA 1D coarsening model was reported to quantitatively predict the coarsening of spherical, or near spherical, carbides on a grain / subgrain boundary during long-term tempering (thousands of hours) in steel [10 - 12]. In the DICTRA model, an initial particle size distribution is assumed, which obeys the Lifshitz-Slyozov-Wagner (LSW) size distribution: the maximum particle size is 1.5 times the average size [13, 14]. The simulation is made by considering a single spherical particle of maximum radius (determined by experimental data) at the centre of a spherical cell determined by the surrounding matrix. The particle is assumed to maintain a spherical shape during the calculation, and the local equilibrium at the curved interface between the particle and the matrix is influenced by the interfacial energy [10]. The interfacial energy contributes to the Gibbs energy function for the particle in the coarsening model through the Gibbs-Thomson effect, Equation 4.

$$\Delta G = \frac{2\lambda V_m}{r} \qquad\qquad \text{Equation 4}$$

Where λ is the interfacial energy; V_m is the particle molar volume, ΔG is the Gibbs energy addition related with the interfacial energy. A particle of maximum size has a smaller Gibbs energy addition compared to the particle of average size, leading to a difference in solute solubility at the interfaces between the matrix and the two particles. This drives diffusion through the matrix and causes the larger particle to grow at the expense of smaller ones [11]. However, when applied to creep resistant steels [10 - 12] the predictions for coarsening of carbides on the grain / subgrain boundaries showed differences with carbide coarsening trends from experimental observations, such as in a Fe-0.11C-8.96Cr-0.47Mo-1.84W-0.2V steel, the measured sizes for MX carbides firstly increased and then decreased with time on tempering at 600 ºC, whereas the DICTRA prediction gave an increase in particle sizes.

The reported theoretical analyses and DICTRA coarsening model use the mean field approach to give descriptions for variation in mean size of particles on grain / subgrain boundaries; as such they cannot deal with changes in the distribution (i.e. DICTRA simulations maintain an LSW distribution). There are many limitations restricting the use of these approaches which are summarised in Table 1. Meanwhile these models also cannot give concurrent information on both coarsening and dissolution of carbides on grain / subgrain boundaries. Therefore the purpose of this study is to develop a mathematical model (based on the finite difference approach) to simulate coarsening and dissolution of coupled inter-lath cementite particles as a continuous and simultaneous process based on experimental carbide characterisation. Once the model is established and validated, it will be capable of predicting the tempering response under different time / temperature schedules for a given starting particle distribution in steels.

Table 1. The strengths and limitations of theoretical approaches and DICTRA model for the coarsening of grain / subgrain boundary particles in steel [2-6, 10-15]

	Strengths	Limitations
Theoretical models	Give a qualitative description	1. Difficult to give quantitative coarsening prediction due to many of the parameters in Equations 1 - 3 being difficult to obtain; 2. The stability of the particle distribution influences the coarsening results in practice that is not incorporated into the theoretical description;
DICTRA coarsening model	1. Gives quantitative coarsening prediction 2. Easily programmed and calculated 3. Deals with cross-element diffusion effects	1) Defined spherical particle shape not necessarily representative; 2) Defined particle size distribution not necessarily representative; 3) Uncertainties of the data used in the kinetic database; 4) Limited number of alloying elements can be dealt with;

2. Material and methods

A laboratory-produced low carbon low alloy Q&T steel plate was supplied by Tata Steel (UK) that had been hot rolled to ~35 mm thickness and air cooled, with the chemical composition given in Table 2. Samples measuring 15 × 20 × 20 mm (15 mm through thickness) were re-austenitised at 925 °C for 1 hour and then quenched into room temperature water, to produce a fully lath martensitic microstructure. Quenched samples were tempered for 2 hrs, 4 hrs, 8 hrs and 16 hrs at 600 °C to investigate carbide coarsening behaviour in this steel. The particle morphology and compositions were examined by scanning electron microscopy (SEM) in a Jeol 7000 system and scanning

transmission electron microscopy (STEM with high angle annular dark field imaging) using an FEI Tecnai F20 system. SEM samples were polished to an OP-S finish and lightly etched in 2% nital. Thin foil specimens used for TEM observations were cut from the mid-thickness position for selected tempered samples, then ground with silicon carbide papers (grit no. 400 - 800 - 1200) to approximately 70 - 80 μm thickness, followed by twin jet electro-polishing with a 5 vol. % perchloric acid and 95 vol. % acetic acid solution at room temperature using 50 - 60 V potential giving a 0.16 - 0.18 A polishing current. Axiovision 4.6.3 image analysis software was used to obtain the particle size (length (major axis) and width (minor axis)) distributions, number densities, volume fractions and particle half-length differences with separations from SEM images (approximately 1000 inter-lath cementite particles measured for each condition assessed). An example showing the measurement of particle half-length differences with separations is shown in Figure 1, where the particle separation refers to the distance between two particles next to each other along lath boundaries. The detailed measurements and annotations of particle areas and separations for cementite in a specific lath boundary were shown in Figure 1 (b), where the particle areas could be converted to particle half-length based on the observations that the inter-lath cementite particles were elliptical in shape along the lath boundaries (2D).

The coarsening / dissolution of inter-lath carbides has been modeled using a 1D finite difference approach coded in Matlab with equilibrium compositions being derived from Thermo-Calc (version 4.1) using TC-Fe7 database.

Table 2. The chemical composition for the low carbon low alloy Q&T steel examined (*wt*%)

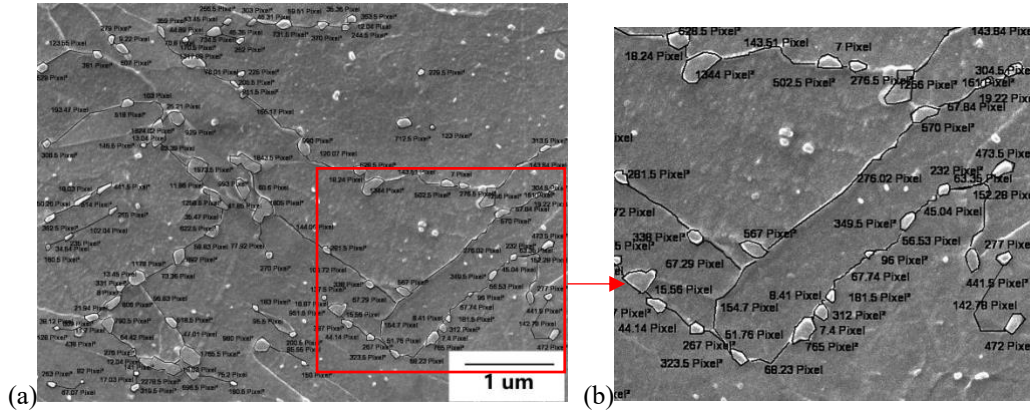| Name	C	Si	Mn	P	S	Al	N	Nb	Ti	B
Base	0.17	0.29	1.2	0.015	0.002	0.03	0.004	0.03	0.024	0.0025

Figure 1. (a) An example showing the measurement of particle half-length differences with separations in this steel; (b) the magnified area from (a) showing a few cementite particles on a specific lath boundary where the particle dimensions and separations are fully annotated.

3. Initial parameters in the simulation

3.1 Schematic diagram for the model

The inter-lath and intra-lath carbides are elliptical in shape in this steel when tempering from 2 hrs to 16 hrs at 600 °C, and were confirmed as cementite by SADP technique (the predicted equilibrium carbide in this steel)[1]. The constant volume fraction has been established after tempering for 2 hrs (around 3.0±0.5% measured experimentally) and agreed with the equilibrium cementite volume fraction in this steel (Thermo-Calc calculation). The cementite volume fraction remained constant (within experiment accuracy) from 2 to 16 hours tempering with the inter-lath and intra-lath cementite fraction also remaining constant. The majority of the overall cementite volume fraction during this range of tempering times was located at inter-lath sites (2.7±0.4%), and these coarsened independently of the intra-lath cementite [1, 16]. Therefore, solute diffusion between cementite particles on tempering from 2 hrs to 16 hrs is either along the lath boundary, resulting in coarsening of inter-lath cementite, or through the bulk, leading to coarsening of intra-lath cementite, but not through the bulk to a boundary [1]. This indicates that coarsening of inter-lath cementite can be simulated independently from that of intra-lath cementite on tempering in this steel.

As shown in Figure 2, the substitutional alloying element Mn is observed to enrich inter-lath cementite in this steel. In terms of consistently checking the Mn content in the inter-lath cementite and ferrite matrix after tempering for different times, the Mn to Fe ratio Y_{Mn} is used as defined in Equation 5.

$$Y_{Mn} = \frac{wt\,(Mn)}{wt\,(Fe)}$$
<div align="right">Equation 5</div>

Where *wt*(Mn) and *wt*(Fe) are the weight percentages of Mn and Fe respectively taken from EDS measurements of inter-lath cementite particles and the ferrite matrix. As listed in Table 3, Mn partitions into inter-lath cementite with a constant content during tempering from 2 hrs to 16 hrs; the measured Y_{Mn} in inter-lath cementite is less than the equilibrium calculated Y_{Mn} in cementite, which may be due to experimental errors (e.g. EDS spot size not being 100% particle or matrix). The results agree well with reported observations and calculations of equilibrium Mn contents in cementite in Fe-0.6C-1Mn and Fe-0.6C-2Mn steels [17]. As Mn is the only substitutional alloying element present in the cementite at detectable levels, Figure 2, and, during coarsening the content of this element is constant, there must be long-range diffusion of Mn through the matrix during tempering. The diffusional flux of other substitutional elements would be low (as if they are present in the cementite it is at levels below the detection limit) or short-range, i.e. if an interfacial layer of Si is present. Hence, it is expected that Mn diffusion between particles will be the rate-controlling step for coarsening of inter-lath cementite. It is also proposed that the equilibrium Mn content in inter-lath cementite is achieved on tempering for 2 hrs and maintained on tempering for 16 hrs, which ensures that there is no extra Mn accumulating inside inter-lath cementite particles to accelerate the simulated coarsening rates.
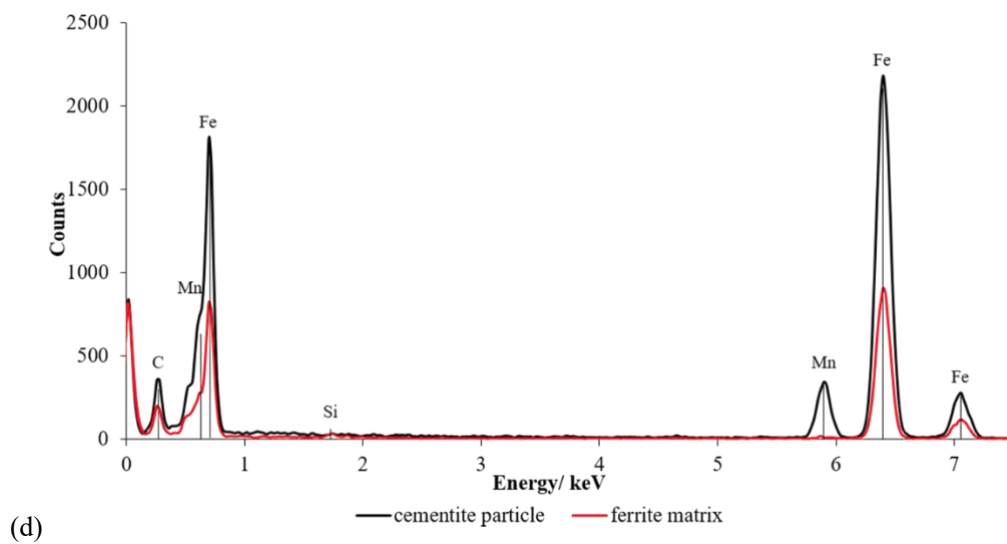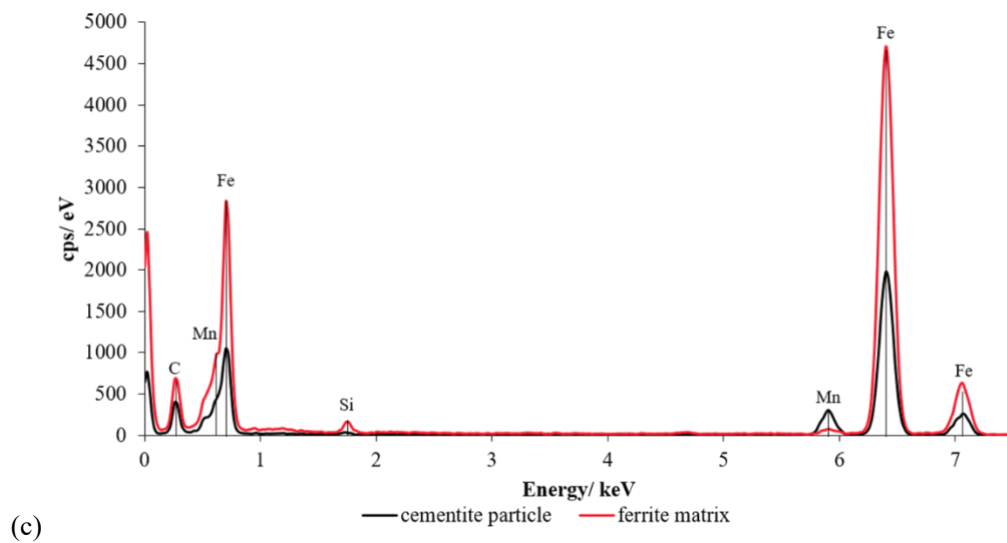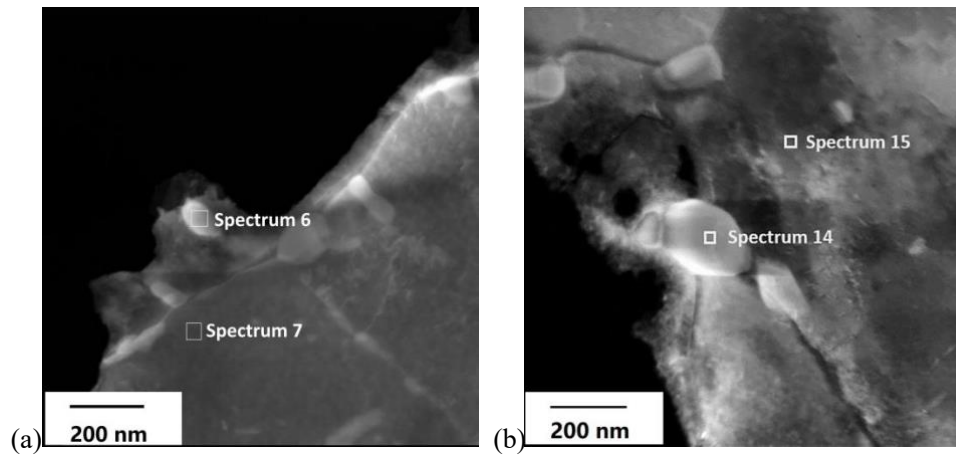
Figure 2. EDS measurements of the chemical composition for inter-lath cementite and the ferrite matrix: the morphology of the selected particle and matrix for EDS measurements are shown in (a)

after tempering for 2 hrs and (b) after tempering for 16 hrs; (c) EDS spectra for inter-lath cementite and the ferrite matrix in (a); (d) EDS spectra for inter-lath cementite and the ferrite matrix in (b).

Table 3. Y_{Mn} for the inter-lath cementite and ferrite matrix after tempering for 2 hrs and 16 hrs from EDS measurements

	2 hrs	16 hrs
Measured Y_{Mn} in inter-lath cementite	0.140±0.016	0.146±0.014
Measured Y_{Mn} in the ferritic matrix	0.012±0.002	0.012±0.003
Thermo-Calc calculated Y_{Mn} in cementite - equilibrium condition	0.188	
Thermo-Calc calculated Y_{Mn} in the ferrite matrix -equilibrium condition	0.009	

The mathematical model for coarsening and dissolution of coupled inter-lath cementite particles, Figure 3, considers the coarsening of a larger particle, A, occurring at the expense of a smaller particle, B. The simulation process covers the half-lengths of particles A and B and the separation between the two particles along the lath boundary. These data replace the particle radius and volume fraction data needed for current mean field-based simulations. The mathematical model is based on the finite difference approach, therefore, suitable length step Δx (along the lath boundary on the line between the particles) and time step Δt values need to be determined for the simulation. The matrix is body centred cubic ferrite after tempering for 2 hrs, as all the excess carbon precipitates from the as-quenched martensitic matrix during the first two hours tempering [1, 16]. The diffusion of Mn between inter-lath cementite particles is considered to be the rate-controlling step in the model, therefore, the length step Δx should be larger than the smallest distance between substitutional positions in a BCC crystal ($\frac{\sqrt{3}}{2}a$, a is the lattice parameter), hence Δx is taken as 0.5 nm in the calculation. The time step Δt is then determined from the stability criterion:

$$D_{LAGB}\frac{\Delta t}{\Delta x^2} \leq \frac{1}{2} \qquad\qquad \text{Equation 6}$$

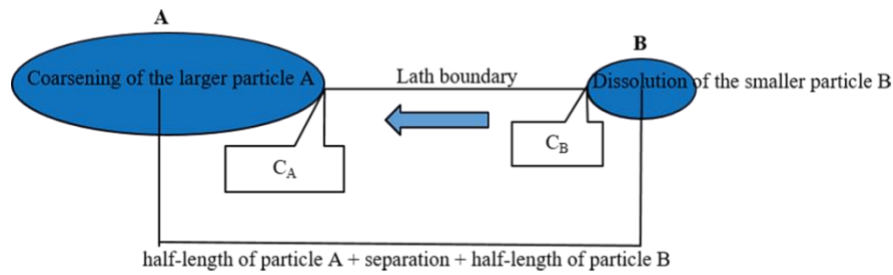Where D_{LAGB} is the Mn diffusivity along the lath boundary.

Figure 3. Schematic diagram for the coupled inter-lath cementite system. C_A and C_B are solute concentrations in the matrix adjacent to particles A and B on the lath boundary. X-axis is the whole distance in the model, which is along the lath boundary on the line between the two particles.

3.2 Initial particle sizes in the model

Based on the previously published work [1], inter-lath cementite particles coarsen faster after tempering from 2 hrs to 4 hrs compared to that after tempering from 4 hrs to 16 hrs at 600 °C. The simulation here was then carried out for inter-lath cementite on tempering from 2 hrs to 4 hrs. As shown in Figure 4, the number density of inter-lath cementite particles significantly decreases for particles with a half-length in the 40 - 100 nm range and increases for particles with a half-length in the 130 - 200 nm range on tempering from 2 hrs to 4 hrs. All carbides in the smallest size range (half-length in the 40 - 50 nm range) have fully dissolved, whereas particles with a half-length in 60 - 90 nm range have partially dissolved during tempering from 2 hrs to 4 hrs at 600 °C. In addition, the size range for largest inter-lath cementite particles increases from a half-length in the 130 - 140 nm range to 190 - 200 nm. Moreover, the effect of carbide separation along lath boundaries should also be taken into consideration for coarsening and dissolution of inter-lath carbides, which is presented in Figure 5. Based on the distribution of coupled inter-lath cementite particles with different separations and half-length differences in Figure 5 (a), the general coarsening direction for coupled inter-lath cementite is ascertained as from larger half-length difference with smaller separation to smaller half-length difference with larger separation (red arrowed). Hence,

coupled inter-lath cementite particles with the largest half-length difference and smallest separation coarsen and dissolve firstly. Most of coupled inter-lath cementite particles with smaller half-length differences and separations remain during tempering, e.g. region of size difference in 0 - 40 nm and separation of 0 - 600 nm. Additionally, the region for coupled inter-lath cementite with largest half-length difference and smallest separation varies with time during tempering, e.g. moving from the region of half-length difference from 90 - 100 nm and separation of 0 - 200 nm after tempering for 2 hrs (indicated by the red rectangle in Figure 5 (b)) to the region of half-length difference from 130 - 140 nm and separation of 0 - 400 nm after tempering for 4 hrs (indicated by the blue rectangle in Figure 5 (b)). This demonstrates the initial condition for simulation on tempering. Hence, coupled particles with the largest half-length difference (between the smallest particles with a half-length of 40 / 50 nm and the largest particle with a half-length of 135 nm) and a separation of 200 nm were firstly selected for simulation on tempering from 2 hrs to 4 hrs in order to consider sensitivity of the dissolution time to the fine particle size, which can then be compared with the experimentally determined particle distributions, as listed in Table 4 (i and ii). In addition, the medium-sized particle with a half-length of 80 nm (in the half-length range of 60 - 90 nm) and the largest particle with a half-length of 135 nm combined with the average (400 nm) / largest (800 nm) separations were also chosen for simulation in terms of further checking the validity of the model on the prediction of dissolution times to a wider size range of particles, Table 4 (iii and iv). In the first two conditions (i and ii) the selected smallest particles should be calculated to dissolve fully, whereas in the last two conditions the half-length for the medium-sized particle is expected to decrease to ≥ 50 nm after simulation based on the experimental observation that all inter-lath cementite particles ≤ 50 nm have fully dissolved after tempering for 4 hrs at 600 °C, Figure 4.
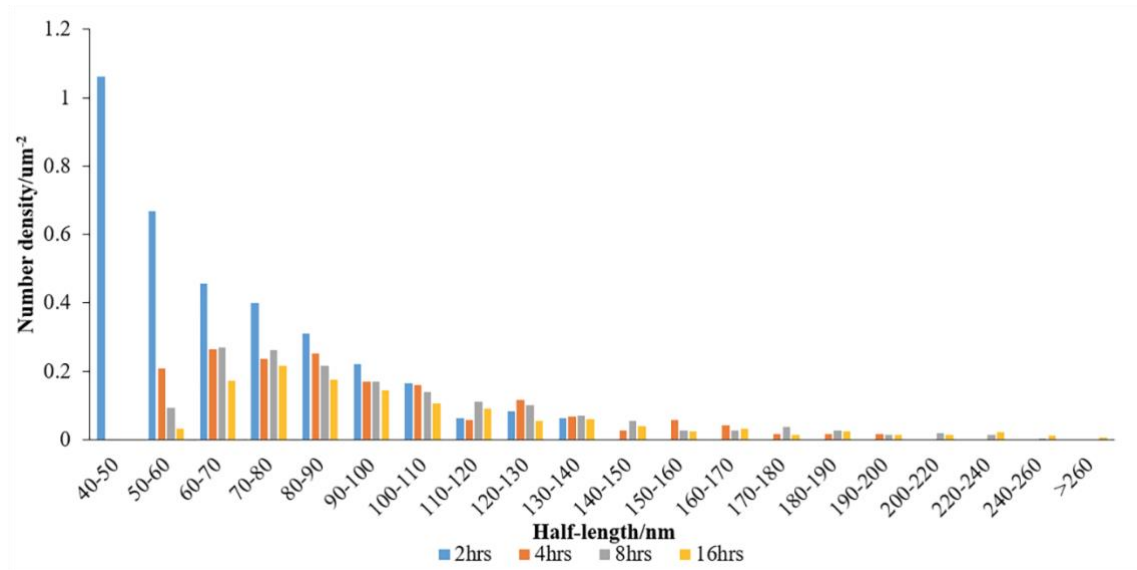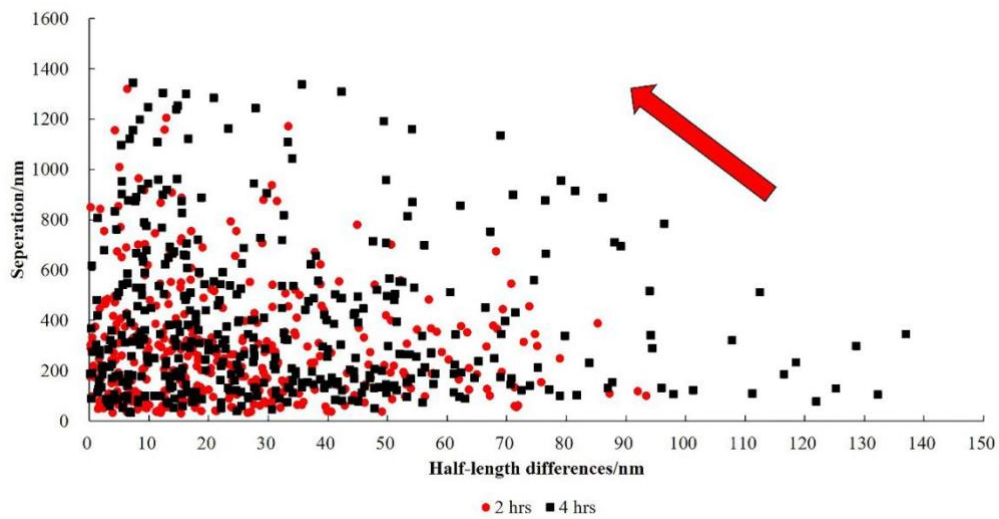
Figure 4. The number density - half-length distribution for inter-lath cementite on tempering from 2 hrs to 16 hrs at 600 °C.

(a)
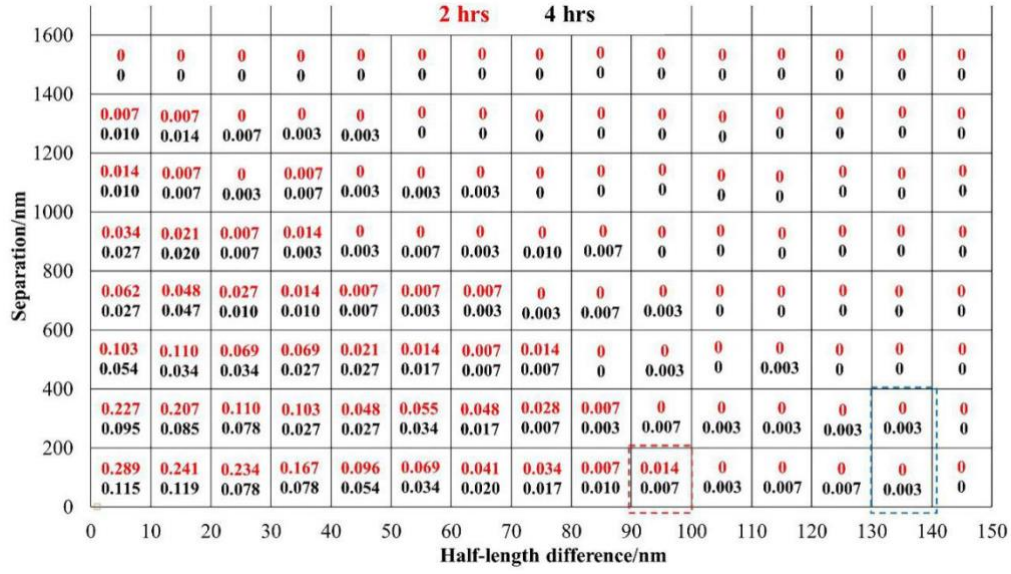
Figure 5. (a) The distribution of coupled inter-lath cementite with different separations and half-length differences after tempering for 2 hrs and 4 hrs at 600 °C; (b) changes of number density for coupled inter-lath cementite with different separations and half-length differences extrapolated from (a). The red and blue rectangles in (b) enclose the particles with largest size differences with smallest separations after tempering for 2 hrs and 4 hrs.

Table 4. Initial parameters used in the simulation for coarsening of inter-lath cementite between 2 hrs and 4 hrs

	Half-length for the coupled inter-lath cementite particles/nm	The adjacent particle separation/ nm	Whole distance for simulation/ nm
i	Particle **A** (half-length 135 nm) + Particle **B** (half-length 40 nm)	200	375
ii	Particle **A** (half-length 135 nm) + Particle **B** (half-length 50 nm)	200	385
iii	Particle **A** (half-length 135 nm) + Particle **B** (half-length 80 nm)	400	615
iv	Particle **A** (half-length 135 nm) + Particle **B** (half-length 80 nm)	800	1015

3.3 Particle shape

The average aspect ratio for all inter-lath carbides remains constant at 1.67±0.01 during tempering for up to 16 hours based on the previously published work [1]. However, when the aspect ratio is considered as a function of inter-lath cementite half-length in Figure 6, there is an approximately linear increase in aspect ratio with increasing half-length for the 2 hour tempered carbides (the low number density of larger particles would explain why this does not cause a change in the average aspect ratio). Likewise the aspect ratio also increases with size for samples on tempering from 2 hrs to 16 hrs, although more significant variation is seen for the larger particles, again attributed to the low number density (therefore the fitting lines in Figure 6 are based on the experimental trend in the small size range extrapolated to give the aspect ratio for particles in the full-size range). Based on the observed aspect ratio values, the inter-lath cementite is confirmed to be elliptical in shape along the lath boundary (2D), therefore, the 3D shape for inter-lath cementite is assumed to be an ellipsoid of revolution with width (2b), length (2a) and height (2a), Figure 7. The length of the particle is along the lath boundary and in the 2D lath boundary plane the particle is circular, which agrees with the particle shape assumption made by others in their theoretical analyses [2 - 4]. The equation of the curvature ρ for the vertex along the length is

$$\rho = \frac{b^2}{a} = \left(\frac{1}{A_s}\right)^2 a \qquad \text{Equation 7}$$

Where A_s is particle aspect ratio, defined as a/b.
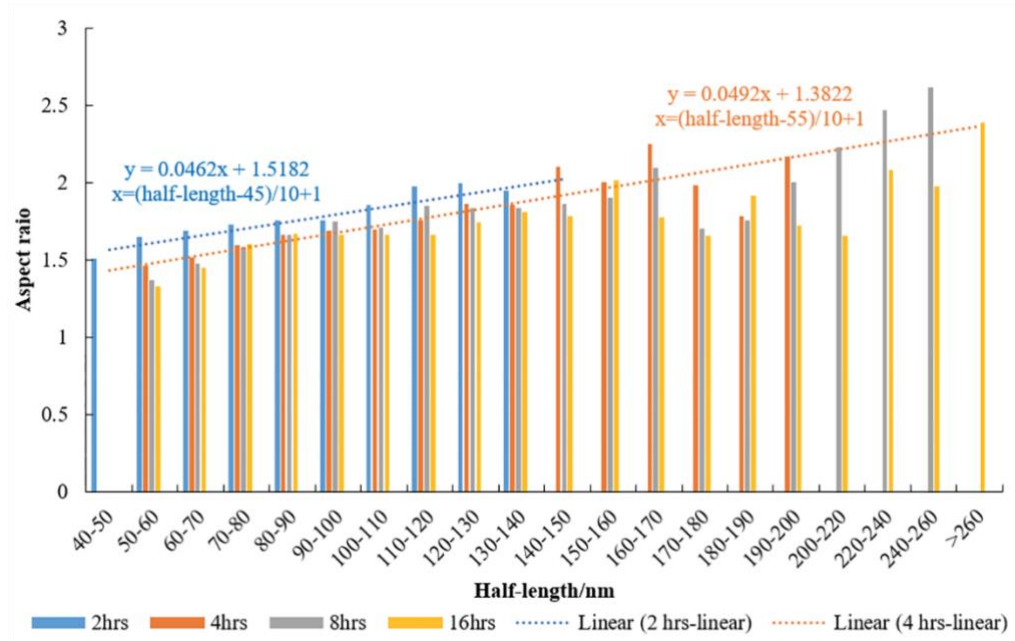
Figure 6. The aspect ratio - half-length distribution for inter-lath cementite during tempering from 2 hrs to 16 hrs. The blue dotted line with equation is the fitted aspect ratio after tempering for 2 hrs; the orange dotted line with equation is the fitted aspect ratio during tempering from 4 hrs to 16 hrs. X in the fitting equations is associated with the half-length value and y is the fitted aspect ratio value.
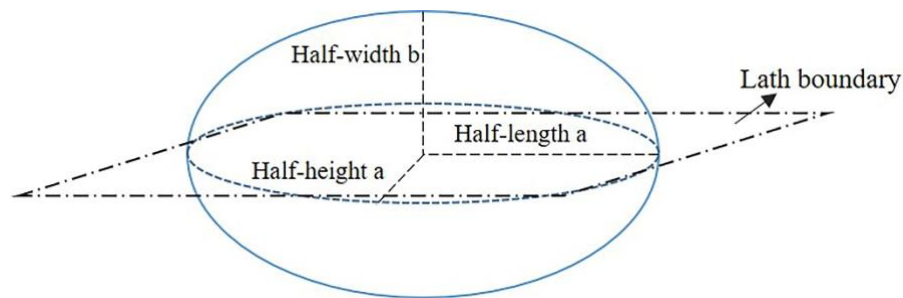
Figure 7. The assumed inter-lath cementite shape in three dimensions.

3.4 Mn concentration profile between coupled inter-lath cementite particles

Mn enriches cementite particles at a level that remains constant for tempering from 2 hrs to 16 hrs (as stated in section 3.1). Hence, diffusion of Mn between the smaller and larger particles in the coupled inter-lath cementite system must take place and, as Mn is substitutional, this is expected to be the rate-controlling step. As the interfaces between cementite and ferrite are curved, there will be additional interfacial energy influencing the equilibrium Mn concentration in the ferrite matrix adjacent to carbide

particles, which is based on the Gibbs-Thomson equation:

$$C_r = C_0 (1 + \frac{2\lambda V_m}{\rho RT})$$
Equation 8

Where C_0 is the equilibrium Mn solubility at a planar interface in the matrix; λ is the cementite/matrix interfacial energy; V_m is the molar volume of the precipitates; ρ is the interfacial curvature of the precipitates. The Mn content in ferrite with no interfacial energy addition from Thermo-Calc is [Mn]=0.860 wt % for this steel at 600 °C. The Mn concentration profile in cementite and the ferrite matrix in the model is shown schematically in Figure 8. The interfacial energy for inter-lath cementite is estimated to be 0.5 J/m$_2$ based on the measured interfacial energy for lenticular-shaped cementite at equilibrium with grain boundaries using the dihedral angle method [18]. The cementite molar volume is calculated as $0.6 \times 10_{-5}$ m$_3$/mol from Thermo-Calc, which is consistent with the reported values in Fe-0.6C steels [15, 17]. The Mn concentrations in the interface elements for both particles (e.g. elements m+n and m in Figure 8) and other matrix elements (e.g. elements from m+1 to m+n-1 in Figure 8) can then be acquired using different particle curvatures in Equation 8: C(A) and C(B) for interface elements are therefore related with ρ_A and ρ_B for particles A and B respectively. For the other matrix elements, a constant value of C(average) is used. The last value is based on the average curvature $\rho_{average}$ ($\rho_{average}$ values are calculated as 23.9 nm, 34.1 nm, 37.7 nm after tempering for 2 hrs, 4 hrs and 16 hrs respectively) which is defined using the average half-length and aspect ratio of the particle distribution to represent the average Gibbs free energy addition for the whole system. The curvature effect is very small inside cementite, therefore, the Mn content inside cementite can be considered to be constant as [Mn]=14.815 wt % obtained from Thermo-Calc calculations.
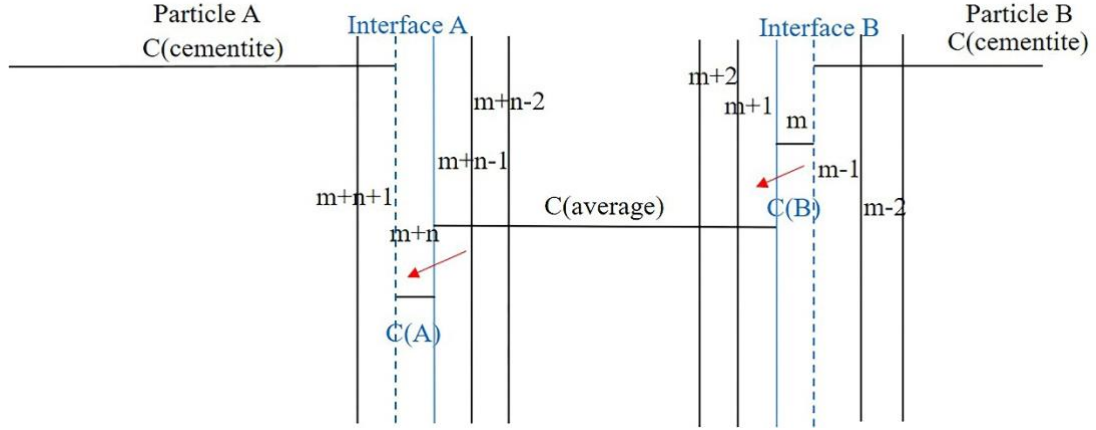
Figure 8. Schematic diagram showing the Mn concentration profile in the matrix and cementite based on Figure 3 considering the different curvatures of the larger (A) and smaller (B) particles. Here, interface elements refer to elements which contain the moved interfaces for both particles, e.g. elements m+n and m are the interface elements for particles A and B respectively in this figure. The red arrows indicate the solute flux between interface elements and their adjacent elements (between m and m+1 / between m+n-1 and m+n).

3.5 Mn lath boundary diffusivity

Mn lath boundary diffusivity has been estimated based on the associated literature [19 - 24], as no available Mn lath boundary diffusivity in the ferrite matrix has been reported. As Mn in the periodic table is next to Fe, then Mn diffusivity along lath boundaries should be similar to the self-diffusivity of Fe along subgrain (e.g. lath) boundaries in ferrite. Based on Gust's evaluations and correlations of grain boundary self-diffusivities proposed in BCC metals (including α-Fe) [22], the self-diffusivity of Fe along grain boundaries in α-Fe is

$$\delta D_{Gb} = 9.2 \times 10^{-14} \exp(-10.4 T_m / T) \qquad \text{Equation 9}$$

where δ is the boundary thickness, 0.5 nm; T_m is the steel melting point, which is calculated as 1452 °C from Thermo-Calc for this steel; T is the tempering temperature 600 °C. The grain boundary self-diffusivity of Fe in ferrite is estimated as 2.16×10^{-15} m²/s at 600 °C. The self-diffusivity of Fe along lath (low-angle) boundaries (D_{LAGB}) in ferrite is assumed to be 2 orders of magnitude lower than that along high-angle grain boundaries (D_{HAGB}) at $T_m/T = 2.42$ based on literature reports for substitutional element diffusivity in BCC metals [23, 24]. Therefore, Mn lath boundary diffusivity in α-Fe,

which is approximately equal to the self-diffusivity of Fe along lath boundaries, is estimated to be 2×10^{-17} m^2/s, which is larger than the reported self-diffusivity of Fe in the ferrite matrix (D_V) (($1 - 2)\times10^{-21}$ m^2/s [19 - 21] at 600 °C, agreeing well with $D_{HAGB}>D_{LAGB}>D_V$. Therefore, $D_{LAGB}(Mn)=2\times10^{-17}$ m^2/s is used in this simulation.

4. Simulation process

The coarsening and dissolution of cementite along lath boundaries occurred under equilibrium cementite volume fraction / composition conditions during tempering from 2 hrs to 16 hrs at 600 °C in this steel. Fick's first law was used to calculate the diffusional flux of solute atoms as Δt was assumed to be small enough for composition change in the model. The finite difference simulation considers fluxes of Mn into and out of each element at successive time steps. The simulation adopted the following stages:

Stage 0. At simulation time t=0 (j=0), the [Mn] levels in elements i=m, m < i < m+n and i=m+n are C(B), C(average), C(A) respectively, Figure 8.

Stage 1. For the first (and the subsequent, i.e. j ≥ 1) time steps, the flux of Mn from the smaller, dissolving particle is initially calculated. For the interface element, m, the fluxes into (from particle B, element m-1) and out of (into matrix, element m+1) are calculated using equations 10 and 11. As there is no source of Mn to replenish that lost by particle B, it dissolves, which is dealt with by the interface moving into the particle, Figure 9 (a). In the initial stages of coarsening, when the composition difference is high and the separation is short, then diffusion through the matrix is rapid (i.e. the Mn diffusion time is less than 1 minute for coupled particles with half-lengths of 135 and 40 nm and separation of 200 nm). This means that volume diffusion through the lath boundary matrix is not rate determining and the assumption can be made that Min and Mout are equal for elements from m to m+n so that Mn is transferred from the smaller to the larger particle without accumulation in the interface elements, i.e. the composition and width of the interface elements remain constant for a single time step.

$$\text{Min(m,j)=Mout(m,j)=-D}_{\text{LAGB}} \frac{C(m+1,j)-C(m,j)}{\Delta x} \Delta t \qquad\qquad \text{Equation 10}$$

$$\text{Mout(m+n,j)=Min(m+n,j)=-D}_{\text{LAGB}} \frac{C(m+n,j)-C(m+n-1,j)}{\Delta x} \Delta t \qquad\qquad \text{Equation 11}$$

Particle A coarsens during these time steps and the fluxes into (from the matrix) and out of (into particle A) the interface element m+n are also calculated. The lesser of the two inward fluxes for elements m and m+n will determine the flux transferred from B to A in that time step (assuming fast enough transit along the lath boundary as discussed above). From this flux minimum, the movement of interface B into element m-1 can be estimated from Equation 12. This equation arises as the interface element maintains its composition (there is little change in particle radius for a single time step so that C(B) is constant and is not raised by accumulation of solute in the interface element; the width of the element is also kept constant). Hence, the Mn released by dissolution of cementite will depend on the difference between the composition of cementite and the matrix. The role of the matrix composition, which depends on the average particle curvature, is not often considered in coarsening simulations. As the fluxes are equal for both particles, then mass balance arguments lead to the corresponding movement of the A interface being described by Equation 13, Figure 9 (b).

$$\Delta d_B(j+1) = \frac{Mmin(j)}{C(cementite)-C(average,j)} \qquad\qquad \text{Equation 12}$$

$$\Delta d_A(j+1) = \Delta d_B(j+1) \times \frac{S_B(j)}{S_A(j)} \qquad\qquad \text{Equation 13}$$

The diffusion of Mn only takes place between interface elements (m or m+n) and the adjacent elements (m+1 or m+n-1), hence, there is no flux in elements from m+2 to m+n-2 (Min=Mout=0). Furthermore, there is also no flux and Mn concentration change for the elements inside cementite particles A and B.
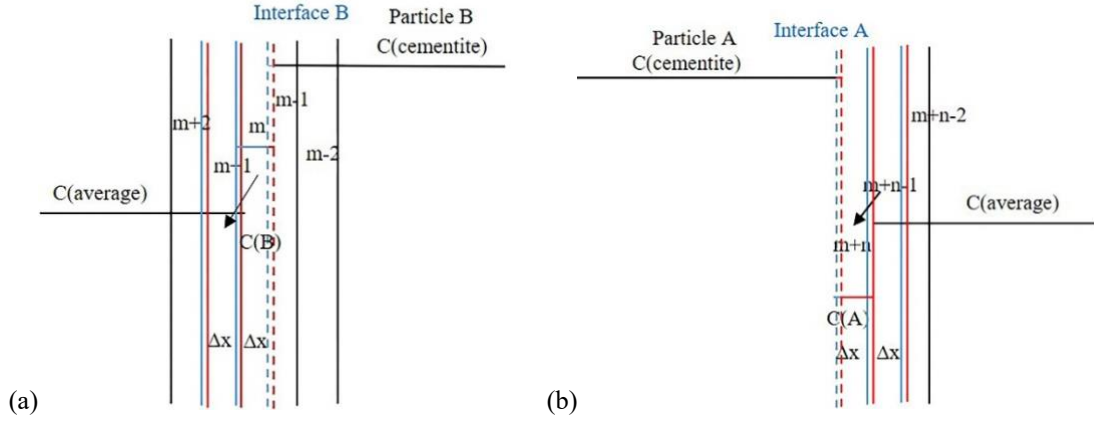
Figure 9. (a) Schematic diagram showing the Mn concentration profile and interface movement around interface B at the time steps j and j+1. The blue lines refer to the position of interface element m and its adjacent element m+1 at the time step j. The red lines refer to the position of interface element m and its adjacent element m+1 at the time step j+1. (b) Schematic diagram showing the Mn concentration profile and interface movement around interface A at the time steps j and j+1. The blue lines refer to the position of interface element m+n and its adjacent element m+n-1 at the time step j. The red lines refer to the position of interface element m+n and its adjacent element m+n-1 at the time step j+1. The black arrows in (a) and (b) indicate Mn fluxes between elements m and m+1 and between elements m+n and m+n-1 respectively.

Stage 2. As the number of time steps increases, then there is a greater movement of the A and B interfaces. If these cumulative values are $< \Delta x$ for both particles then radius changes are small enough that aspect ratio, C(A), C(B) and C(average) are not changed, i.e. at time step j=p, the Mn concentrations in the interface elements m and m+n remain constant as C(m,p)=C(m,p-1) and C(m+n,p)=C(m+n,p-1); meanwhile, C(average,p)=C(average,p-1). As the interfaces move with time, the interface elements (m or m+n) and adjacent elements (m+1 or m+n-1) shift as well, but the lengths of these elements remain Δx, indicated by blue lines in Figure 10. However, the boundaries between elements m+2 and m+3 and between elements m+n-2 and m+n-3 remain stationary with time so that the length for m+2 increases ($>\Delta x$) and for m+n-2 decreases ($<\Delta x$), as indicated by the purple arrows in Figure 10. The stationary boundaries between elements m+2 and m+3 and between m+n-2 and m+n-3 do not influence the modelling process as there is no flux in elements from m+2 to m+n-2 (Min=Mout=0). The interface motion for particle B at this time step j=p ($\Delta d_B(p+1)$) can be obtained

using Equation 12 using the minimum Mn diffusional flux between particles A and B. Based on the mass balance between the two particles, the interface motion for particle A ($\Delta d_A(p+1)$) is acquired in Equation 13.
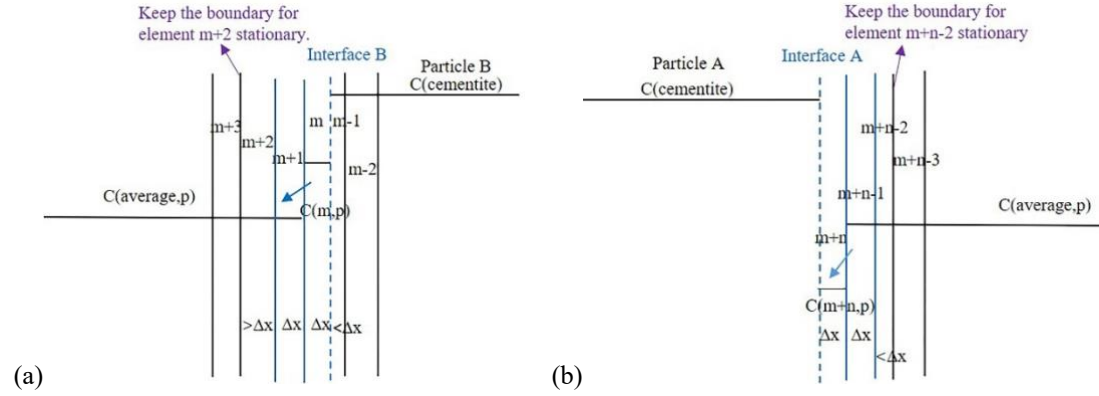

Figure 10. (a) Schematic diagram showing the Mn concentration profile around interface B at time step j=p when the interface B motion < Δx. (b) Schematic diagram showing the Mn concentration profile around interface A at time step j=p when the interface B motion < Δx. The blue dashed lines represent the interface positions for both particles at time step j=p.

Step 3. As the number of time steps increases, then a point will be reached at time step j=q when the particle B / matrix interface has moved by a total increment of Δx to coincide with the boundary between elements m-1 and m-2, Figure 11. As the interface B coincides with the boundary between elements m-1 and m-2, the interface element shifts from element m to m-1 at this time step. The aspect ratio for particle B is also changed at this time step to that corresponding to the new radius, resulting in modifications to the solute concentrations in the interface elements. The interface composition C(m-1,q) for particle B at this time step slightly increases compared to the previous interface composition C(m,q-1) based on the newly-changed half-length and aspect ratio at this time step using Equation 8. Hence, extra Mn from particle B is needed to increase the Mn concentration in element m-1, indicated by the yellow rectangular filled box in element m-1 in Figure 11, which is defined as $\Delta M_B(q)$ in Equation 14. The Mn concentration in matrix elements (except for the interface elements) C(average,q) at this time step decreases compared to that at previous time steps. This is a mean-field parameter, leading to this model being a combination of

mean-field approach and finite difference approach for coupled cementite particles along the lath boundary in terms of being predictive enough to compare with the experimental data. The decreased amount of Mn from the other matrix elements $\Delta M(average,q)$, defined in Equation 15, is assumed to be redistributed to contribute to coarsening of particle A as the solute diffusion direction is from elements with higher concentrations to elements with lower concentrations in the model and back diffusion is assumed not to take place, indicated by the green filled box in Figure 11. In addition, $C(m,q)$ is equal to $C(average,q)$ at this time step.

$$\Delta M_B(q)=[C(m-1,q)-C(m,q-1)]\Delta x \qquad \text{Equation 14}$$

$$\Delta M(average,q)=\Delta C(average,q)[d(separation)+\sum\Delta d_B-\sum\Delta d_A-2\Delta x] \qquad \text{Equation 15}$$

The flux from interface B now occurs between elements m-1 and m

$$M_{in}(m-1,j)=M_{out}(m-1,j)=-D_{LAGB}\frac{C(m,j)-C(m-1,j)}{\Delta x}\Delta t \qquad \text{Equation 16}$$

There are two possible situations for the interface of particle A. One situation is that interface A has moved by an increment $< \Delta x$ in length, Figure 11 (a); the Mn concentration $C(m+n,q)$ in the interface element for particle A remains constant at the value used for previous time steps, and the flux $M_{out}(m+n,q)$ for interface A is acquired from Equation 11. Hence, the interface motion for particle B at time step j=q+1 is composed of two parts: one is due to the minimum amount of Mn diffusional flux $(\Delta d_{B1}(q+1))$; the other is due to the solute redistribution in element m-1 $(\Delta d_{B2}(q+1))$, as defined in Equation 17. The interface movement for both particles is continuous (seen in steps 1 and 2) based on the minimum Mn flux and only differs when non-continuous composition variation for the interface elements and/or other matrix elements occurs.

$$\Delta d_B(q+1)=\Delta d_{B1}(q+1)+\Delta d_{B2}(q+1)$$

$$\Delta d_{B1}(q+1)=\frac{M_{min}(q)}{C(cementite)-C(average,q)} \qquad \text{Equation 17}$$

$$\Delta d_{B2}(q+1)=\frac{\Delta M_B(q)}{C(cementite)-C(average,q)}$$

The interface motion for particle A at time step j=q+1 also consists of two parts: the first part is due to the mass balance between the two particles (minimum Mn flux induced) $\Delta d_{A1}(q+1)$, which keeps consistent with steps 1 and 2; the second part is based on the solute redistribution in matrix elements from m to m+n-1 (except for the interface

elements), which is given by $\Delta d_{A2}(q+1)$, Equation 18:

$$\Delta d_A(q+1)=\Delta d_{A1}(q+1)+\Delta d_{A2}(q+1)$$

$$\Delta d_{A1}(q+1)=\Delta d_{B1}(q+1)\times\frac{S_B(q)}{S_A(q)}$$

$$\Delta d_{A2}(q+1)=\frac{\Delta M(average,q)}{C(cementite)-C(m+n,q)}$$

Equation 18

The other situation is that the interface for particle A moves by an increment of Δx to coincide with the boundary between elements m+n-1 and m+n-2, Figure 11 (b). The aspect ratio for particle A changes; meanwhile, the Mn concentration in the interface element m+n-1 C(m+n-1,q) for particle A decreases due to the newly-changed half-length and aspect ratio. Hence, there is some Mn redistributed in the interface element m+n-1, contributing to coarsening of particle A, as indicated by the purple filled box in element m+n-1 in Figure 11 (b), which is defined as $\Delta M_A(q)$.

$$\Delta M_A(q)=[C(m+n,q-1)-C(m+n-1,q)]\Delta x$$

Equation 19

The flux from interface A now occurs between m+n-1 and m+n-2 and is

$$Mout(m+n-1,j)=Min(m+n-1,j)=-D_{LAGB}\frac{C(m+n-1,j)-C(m+n-2,j)}{\Delta x}\Delta t$$

Equation 20

At j=q time step, C(m+n-2,q)=C(average,q). The interface motion for particle B at time step j=q+1 is acquired from Equation 17. The interface motion for particle A due to the mass balance is the same as $\Delta d_{A1}(q+1)$ in Equation 18, However, $\Delta d_{A2}(q+1)$ is slightly different in this situation due to the assumption that all the excess Mn from the change in C(average,q) goes to particle A. Hence $\Delta d_{A2}(q+1)$ is defined as:

$$\Delta d_{A2}(q+1)=\frac{\Delta M_A(q)+\Delta M(average,q)}{C(cementite)-C(m+n-1,q)}$$

Equation 21

The interface motion for particle A is the sum of $\Delta d_{A1}(q+1)$ and $\Delta d_{A2}(q+1)$.

The above steps are iterated as the interfaces for particles A and B move with increasing time until the total interface motion for particle B is equal to its half-length and the particle dissolves completely.

Figure 11. Schematic diagram showing the Mn concentration profile at time step j=q when the particle B / matrix interface moves by a Δx increment to coincide with the boundary between elements m-1 and m-2: (a) the interface for particle A moves an increment < Δx in length; (b) the interface for particle A moves by a total Δx increment to coincide with the boundary between elements m+n-1 and m+n-2. The blue dashed lines represent the interface positions for both particles at time step j=q. The green dashed lines refer to the Mn concentration C(average, q-1) in other matrix elements (except for the interface elements) at time step j=q-1. The yellow filled boxes are the amount of solute redistribution in element m-1 due to the interface composition variation for particle B. The green filled boxes are the amount of solute redistribution due to the decrease of C(average) contributing to coarsening of particle A. The purple filled box in (b) is the amount of solute redistribution in element m+n-1 due to the interface composition variation for particle A. The red rectangles enclose the interface elements and their adjacent elements.

5. Simulation results and discussion

The simulated interface motions for the larger particle A with half-length of 135 nm and smaller particle B with half-length of 40 nm with a separation of 200 nm in 2 hours at 600 °C (from 2 hrs to 4 hrs total tempering time) are shown in Figure 12 (a) (b). The predicted time for the dissolution of particle B with interfacial energy 0.5 J/m$_2$ is approximately 24 minutes (less than 2 hours), however, the interface motion for particle A is about 1.4 nm due to the dissolution of a single particle B. In addition, the predicted dissolution time for the smaller particle B with half-length of 50 nm is about 38 minutes in the coupled inter-lath cementite system (particle A with half-length of 135 nm and particle B with half-length of 50 nm with a separation of 200 nm), Figure 12 (c); while, the interface for particle A moves around 2.6 nm at the expense of a single particle B with half-length of 50 nm, Figure 12 (d). The predicted dissolution times for the smaller particles with half-length of 40 / 50 nm are in good agreement with experimental data that particles with half-length ≤ 50 nm are all dissolved on tempering from 2 hrs to 4 hrs at 600 °C. However, the calculated coarsening of the larger particle A with half-length of 135 nm cannot achieve the experimentally observed largest size after 4 hours tempering with a single smaller particle consumed.

(a)

(b)

(c)

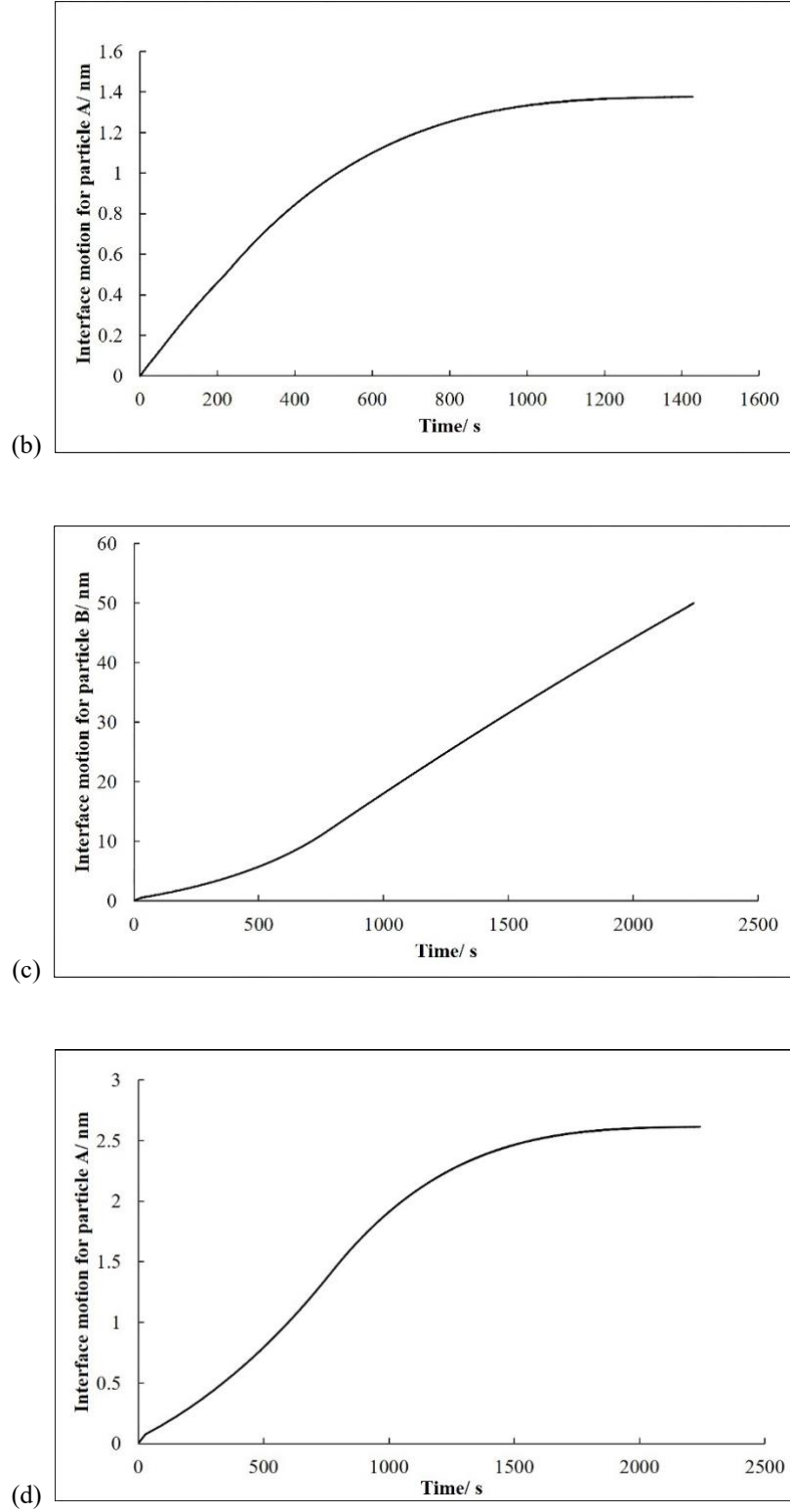(d)
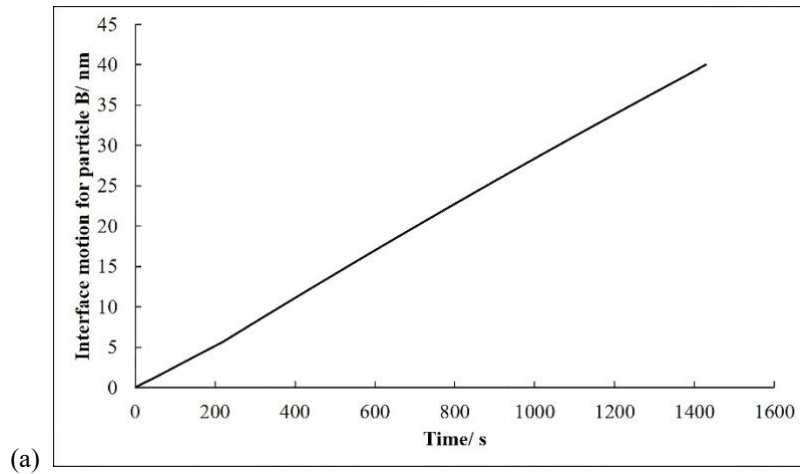
Figure 12. Simulated interface motion for coupled inter-lath cementite systems: (a) particle B with half-length 40 nm and (b) particle A with half-length 135 nm with a separation of 200 nm during tempering from 2 hrs to 4 hrs at 600 °C; (c) particle B with half-length 50 nm and (d) particle A with half-length 135 nm with a separation of 200 nm during tempering from 2 hrs to 4 hrs at 600 °C.

The simulated interface motions for the coupled inter-lath cementite system with the larger particle A with half-length of 135 nm and the medium-sized particle B with half-length of 80 nm with a separation of 400 / 800 nm are shown in Figure 13. As discussed in section 3.4, C(average) is calculated based on the average half-length and aspect ratio; after tempering for 2 hrs, the average half-length is 66.7 nm, which is smaller than the half-length for medium-sized particle B, resulting in C(average) > C(B). There is initially no composition gradient from the medium-sized particle B to the matrix, leading to that the medium-sized particles are kinetically stable until the smaller ones have dissolved and the matrix composition is raised. Therefore, the medium-sized particle B with half-length of 80 nm cannot dissolve on tempering until the average half-length increases to larger than 80 nm. The time needed for the increase of the average half-length to ≥ 80 nm is 0.85 hrs (stared from 2 hrs) based on the mean-field prediction; therefore, the simulation time for this coupled system is about 1.15 hrs. As shown in Figure 13 (a), the medium-sized particle B has shrunk with the half-length decreasing to 52.8 nm in this time region, remaining consistent with the experimental observations that the smallest particles after tempering for 4 hrs locate in the half-length range of 50 - 60 nm. However, the interface motion for the larger particle A moves around 6.4 nm, shown in Figure 13 (b). In addition, different separations in this coupled inter-lath cementite system do not influence the dissolution times of the medium-sized particle B too much, where the predicted interface motion lines in Figure 13 (a) are nearly overlapped due to the assumption that the diffusion of Mn has occurred between the interface elements and their adjacent elements in this model.
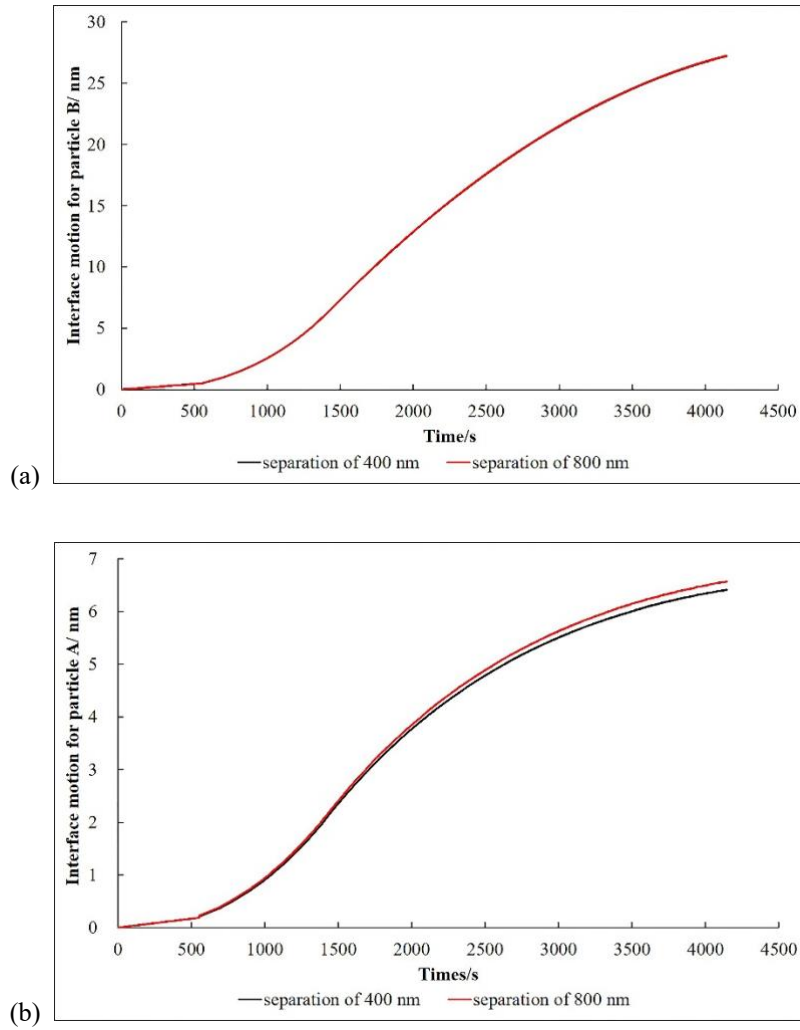
(a)

(b)

Figure 13. Simulated interface motion for coupled inter-lath cementite systems: (a) particle B with half-length 80 nm and (b) particle A with half-length 135 nm with a separation of 400 nm (black line) and 800 nm (red line) during tempering from 2 hrs to 4 hrs at 600 °C.

An assessment of the coarsening of larger particles was carried out based on different particle arrangements on tempering from 2 hrs to 4 hrs. As shown in Figure 4, there is a significant number density decrease for particles with half-length in 40 - 60 nm range for tempering from 2 hrs to 4 hrs; hence, there should be enough smaller particles dissolving to supply Mn to allow the largest inter-lath cementite particle coarsening from half-length 130 - 140 nm to half-length 190 - 200 nm. The amount of Mn released from dissolution of smaller particles with half-length in the 40 - 60 nm range is about 1.03×10^{-17} mol, which is much larger than the required amount of Mn (3.29×10^{-18} mol) for the largest particles to increase in half-length from 130 - 140 nm to 190 - 200

nm. Figure 14 shows the number density variation for coupled inter-lath cementite particles where one particle in the pair has a half-length in the 40 - 60 nm range after tempering for 2 hrs. The largest number density (0.766 μm^{-2}) for coupled particles is located in the region of half-length difference of 0 - 20 nm with a separation of 0 - 400 nm, which occupies about 45% of the overall number density. This means that particles with half-length in the 40 - 60 nm range have the maximum probability to be next to particles with similar sizes. Meanwhile, coupled particles in the region of half-length difference in the 80 - 100 nm range with a separation of 0 - 400 nm have comparatively lower number density (0.028 μm^{-2}) compared to other groupings in Figure 14. The number density ratio between coupled particles in the half-length difference of 0 - 20 nm with a separation of 0 - 400 nm region and coupled particles in the half-length difference of 80 - 100 nm with a separation of 0 - 400 nm region is about 27.4 (0.766/0.028), which indicates that the larger particles with half-length of 130 - 140 would need to be surrounded by up to 28 smaller particles with half-length of 40 - 60 nm in the lath boundary plane. From this arrangement, these smaller particles with half-length 50 nm can dissolve fully to supply Mn (the released Mn amount=1.97×10^{-16} mol) for particle A to coarsen from half-length 135 nm to half-length 195 nm (the required Mn amount=1.94×10^{-16} mol), where the theoretical requirement of mass balance is achieved in practice for particle coarsening and dissolution. Smaller particles with half-length < the initial average half-length are expected to dissolve firstly before the medium-sized particles with half-length > the initial average half-length start to dissolve on tempering from 2 hrs to 4 hrs. Moreover, these medium-sized particles have also dissolved to supply Mn for the coarsening of larger particles, hence, it is likely that there is a mix of small and medium particles surrounding a larger particle supplying Mn for coarsening of the larger particle, and also supplying Mn to other nearby large particles. Based on the simulation results in Figure 12 (d), the interface motion for the larger particle A with half-length of 135 nm is around 73 nm in total after consuming 28 particles of half-length 50 nm with 2 hours tempering time, which is consistent with the observed largest particle size with half-length of 190 - 200 nm after tempering for 4 hrs as shown in Figure 4. Actually, growth of the larger particle fed from several

smaller ones should increase the rate of dissolution / growth and would need the initial 1D simulation to be expanded to 2D simulation.

Number density / μm⁻²

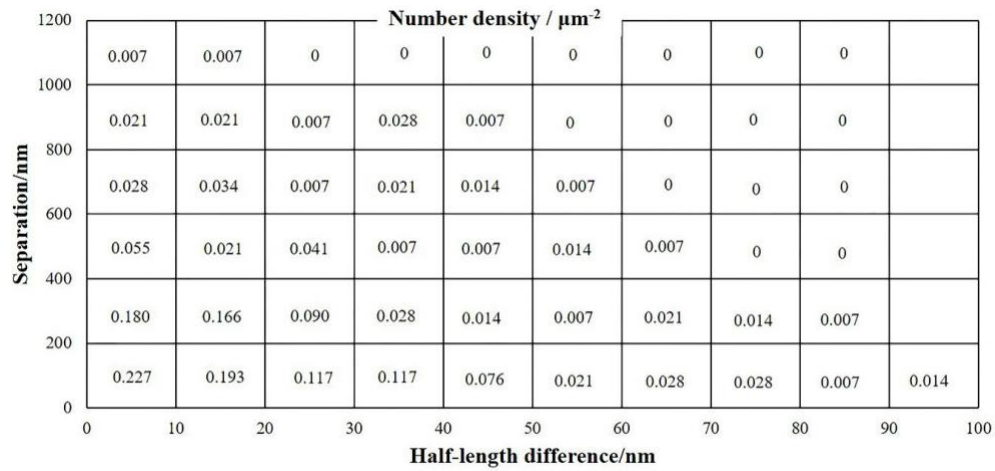| Separation/nm \ Half-length difference/nm	0–10	10–20	20–30	30–40	40–50	50–60	60–70	70–80	80–90	90–100
1000–1200	0.007	0.007	0	0	0	0	0	0	0	
800–1000	0.021	0.021	0.007	0.028	0.007	0	0	0	0	
600–800	0.028	0.034	0.007	0.021	0.014	0.007	0	0	0	
400–600	0.055	0.021	0.041	0.007	0.007	0.014	0.007	0	0	
200–400	0.180	0.166	0.090	0.028	0.014	0.007	0.021	0.014	0.007	
0–200	0.227	0.193	0.117	0.117	0.076	0.021	0.028	0.028	0.007	0.014

Figure 14. The number density variation for coupled inter-lath cementite particles where one particle in the pair has a half-length in the 40 - 60 nm range after tempering for 2 hrs at 600 °C.

As enclosed by the red rectangles in Figure 15(a) (b), the larger particles are situated adjacent to smaller particles with half-length < 50 nm, where the solute 1D diffusion occurs from the smaller particles to the larger particles along the lath boundary (Figure 15(c) - 1 and 2). These smaller particles disappear along the lath boundary within 2 hours (on tempering from 2 hrs to 4 hrs), shown in Figure 16, and the surviving larger particles fall into the half-length category of 190 - 200 nm after tempering for 4 hrs (purple arrows in Figure 16). In addition, multi-particles in different size ranges around the larger particles are also observed after tempering for 2 hrs, enclosed by the green rectangles in Figure 15 (a) (b), where solute diffusion occurs in the reversed directions along the lath boundary (Figure 15 (c)-1 and 3). Hence, a multi-sized inter-lath cementite model is needed in the future based on the established mathematical model for the coupled inter-lath particle system in terms of simulating the coarsening of larger particles and dissolution of smaller particles in the full size range concurrently.
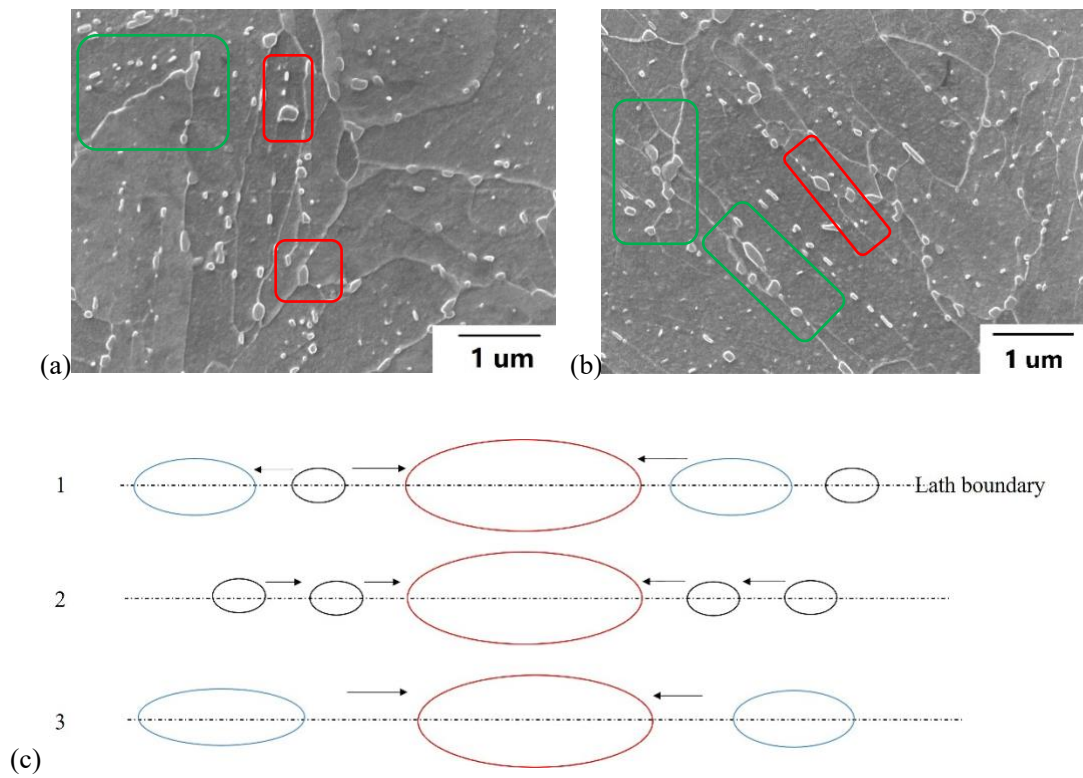
Figure 15. (a) (b) Examples of the observed particle arrangements around larger particles along the lath boundary after tempering for 2 hrs at 600 °C. The red rectangles indicate the largest - smallest particle arrangement and the green rectangles indicate the arrangement of multi-particles in different size ranges. (c) Illustration of particle arrangement along the lath boundary, where red, dark and blue ellipses represent larger particles, smaller particles and particles with medium sizes respectively. The arrows indicate the solute diffusion along lath boundaries.
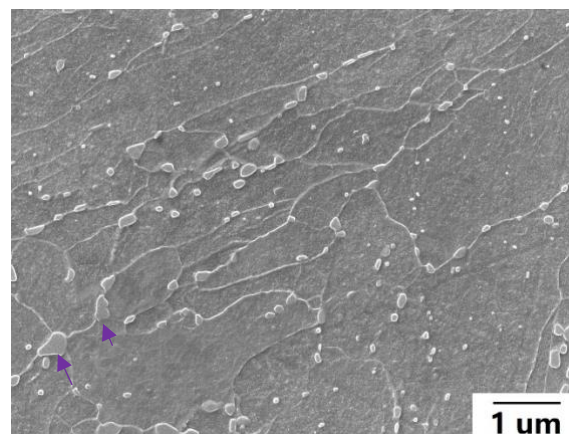
Figure 16. Example of the observed particle arrangements along lath boundaries after tempering for 4 hrs at 600 °C. Purple arrows indicate the larger particles with a half-length of approximately 190 - 200 nm.

6. Conclusions

A mathematical model using the finite difference approach with some parameters, like calculation time, obtained from mean field approach has been established for coupled inter-lath cementite systems based on experimental observations on tempering at 600 °C in a low carbon low alloy Q&T steel, where dissolution of a smaller particle and coarsening of a larger one is treated as a continuous and simultaneous process in the model. The main conclusions are:

(1) Mn 1D diffusion occurs between the interface (spatial) elements and their adjacent (spatial) elements in this model, where the amounts of Mn diffusing into / out of the elements are equal to ensure no accumulation of Mn in the interface elements.

(2) The mathematical model predicts the dissolution times for smaller particles in coupled smaller - larger particle systems, where the predictions fit well with experimental observations for 2 to 4 hours tempering. However, the size increase for the larger particle is predicted to be very small due to the dissolution of a single smaller particle in the model compared to the much larger observed size increase.

(3) Particle arrangements are assessed and considered to verify the prediction on coarsening of larger particles. There is a maximum potential for smaller particles to be located next to similar-sized particles, which cannot coarsen or dissolve, and larger particles tend to be surrounded by smaller ones along lath boundaries after tempering for 2 hrs. The simulated smaller - larger particle arrangement does appear in SEM images after tempering for 2 hrs, and the verified particle coarsening keeps consistent with the observed size increase. In addition, many particles with different size ranges along the lath boundary are also observed, where a multi-particle configurations on lath boundaries are required for full representation.

Reference

[1] Ju Y, Goodall A, Strangwood M, et al. Characterisation of precipitation and carbide coarsening in low carbon low alloy Q&T steels during the early stages of tempering. Mater Sci and Eng A. 2008; 738: 174-189.

[2] Speight MV. Growth kinetics of grain-boundary precipitates. Acta Metall. 1968; 16: 133-135.

[3] Kirchner HOK. Coarsening of grain-boundary precipitates. Metall Trans. 1971; 2: 2861-2864.

[4] Ardell AJ. On the coarsening of grain boundary precipitates. Acta Metall. 1971; 20: 601-609.

[5] Ardell AJ. The effect of volume fraction on particle coarsening: theoretical consideration. Acta Metall. 1972; 20: 61-71.

[6] Enomoto Y, Okada A. Many-body effects on the coarsening of grain boundary precipitates. J Phys: Condensed Matter. 1990; 2: 6275-6278.

[7] Lindsley BA, Marder AR. The morphology and coarsening kinetics of spheroidized Fe-C binary alloys. Acta Mater. 1998; 46: 341-351.

[8] Nam WJ, Bae CM. Coarsening behaviour of cementite particles at a subcritical temperature in a medium carbon steel. Scr Mater. 1999; 41: 313-318.

[9] Nam WJ. Effect of initial microstructure on the coarsening behavior of cementite particles. ISIJ Int. 1999; 39: 1181-1187.

[10] Gustafson Å, Hättestrand M. Coarsening of precipitates in an advanced creep resistant 9% chromium steel - quantitative microscopy and simulations. Mater Sci and Eng A. 2002; 333: 279-286.

[11] Prat O, Garcia J, Rojas D, et al. Investigations on the growth kinetics of Laves phase precipitates in 12% Cr creep-resistant steels: experimental and DICTRA calculations. Acta Mater. 2010; 58: 6142-6153.

[12] Prat O, Garcia J, Rojas D, et al. Investigation on coarsening of MX and $M_{23}C_6$ precipitates in 12% Cr creep resistant steels assisted by computational thermodynamics. Mater Sci and Eng A. 2010; 527: 5976-5983.

[13] Lifshitz IM, Slyozov VV. The kinetics of precipitation from supersaturated solid solutions. J Phys Chem Solids. 1961; 19: 35-50.

[14] Wagner C. Theorie der Alterung von Niederschlägen durch Umlösen (Ostwald-Reifung), Zeitschrift für Elektrochemie, Berichte der Bunsengesellschaft für physikalische Chemie. 1961; 65: 581-591.

[15] Ghosh S. Rate-controlling parameters in the coarsening kinetics of cementite in Fe–0.6 C steels during tempering, Scr Mater. 2010; 63: 273-276.

[16] Ju Y, Goodall A, Strangwood M, et al. Characterisation of precipitation and coarsening of carbides during tempering in a low alloyed quenched and tempered steel. Mater Sci Forum. 2018; 941: 33-38.

[17] Miyamoto G, Oh JC, Hono K, et al. Effect of partitioning of Mn and Si on the growth kinetics of cementite in tempered Fe–0.6 mass% C martensite. Acta Mater. 2007; 55: 5027-5038.

[18] Martin AG, Sellars CM. Measurement of interfacial energy from extraction replicas of particles on grain boundaries. Metallogr. 1970; 3: 259-273.

[19] Hettich G, Mechrer H, Maier K. Self-diffusion in ferromagnetic α-iron. Scr Metall. 1977; 11: 795-802.

[20] Iijima Y, Kimura K, Hirano K. Self-diffusion and isotope effect in α-iron. Acta Metall. 1988; 36: 2811-2820.

[21] Huang S, Worthington DL, Asta M, et al. Calculation of impurity diffusivities in α-Fe using first-principles methods. Acta Mater. 2010; 58: 1982-1993.

[22] Gust W, Mayer S, Bögel A, et al. Generalized representation of grain boundary self-diffusion data. J de Phys Colloq. 1985; 46(C4): 537-544.

[23] Balluffi RW. Grain boundary diffusion mechanisms in metals. Metall Trans B. 1982; 13B: 527-553.

[24] Kaur I, Gust W, Kozma L. Handbook of grain and interphase boundary diffusion data. Milwaukee: Ziegler Press; 1989.